

## Numerical Simulations of Type-III Solar Radio Bursts

B. Li, P. A. Robinson, and I. H. Cairns

*School of Physics, University of Sydney, New South Wales 2006, Australia*

(Received 18 September 2005; published 13 April 2006)

The first numerical simulations are presented for type-III solar radio bursts in the inhomogeneous solar corona and interplanetary space, that include microscale quasilinear and nonlinear processes, intermediate-scale driven ambient density fluctuations, and large scale evolution of electron beams, Langmuir and ion sound waves, and fundamental and harmonic electromagnetic emission. Bidirectional coronal emission is asymmetric between the upward and downward directions, and harmonic emission dominates fundamental emission. In interplanetary space, fundamental and/or harmonic emission can be important. Langmuir and ion sound waves are bursty and the statistics of Langmuir wave energy agree well with the predictions of stochastic growth theory.

DOI: [10.1103/PhysRevLett.96.145005](https://doi.org/10.1103/PhysRevLett.96.145005)

PACS numbers: 96.60.Tf, 52.65.-y, 96.50.Vg

Type-III solar radio bursts discovered 60 years ago, are the most intensively studied form of solar system radio emissions [1]. *In situ* observations show that beam electrons produced during solar flares are the energy source, streaming outward from the sun to interplanetary (IP) space and driving Langmuir waves and radio emission via the plasma emission mechanism [1]. The bursts have fast downward frequency drift, and emission at the electron plasma frequency and/or its second harmonic. Bidirectional coronal type-III bursts have also been observed [2], consisting of components that frequency drifts both upward and downward from a common origin, indicating beams are injected both inward and outward from a compact region. Plasma emission is also responsible for other solar and IP radio emissions [3], e.g., type-II solar bursts, vital to predict space weather and its effects on power, communication, and other technology systems.

Langmuir waves observed in type-III (and type-II) sources are extremely bursty, inconsistent with standard textbook scenarios in which waves simply grow exponentially before saturation. Thus alternative theories including stochastic growth theory (SGT) have been proposed. In SGT [4], density irregularities induce random growth, so Langmuir waves are generated stochastically and quasilinear interaction within these Langmuir clumps causes the beam to fluctuate about marginal stability. SGT has predicted a hierarchy of regimes and proved successful in a variety of systems in space physics and astrophysics [e.g., Langmuir waves in type-III sources and Earth's foreshock, electromagnetic ion cyclotron and mirror waves in Earth's magnetosheath, solar spike bursts, and pulsar emission [4]]. The first aim of this Letter is to demonstrate that type-III burst is a SGT system which can thus serve as an

archetype of the SGT systems. Because of the almost universal burstiness of waves observed in the space and astrophysical context, the study of type-III bursts thus has important implications on other complex systems with SGT behavior.

Significant advances in theoretical modeling type-III bursts have been made recently. One semiquantitative theory for type-III bursts via plasma emission involves the following steps [5]: (i) the beam generates primary Langmuir waves  $L$  by a beam instability; (ii)  $L$  waves undergo electrostatic (ES) decay  $L \rightarrow L' + S$  to generate product Langmuir waves  $L'$  and ion sound waves  $S$ ; (iii)  $S$  waves stimulate the  $L$  waves to produce fundamental transverse waves  $F$  via electromagnetic (EM) decay  $L \rightarrow F + S$ ; and (iv)  $L$  wave pairs coalesce to generate second harmonic transverse waves  $H$  via  $L + L' \rightarrow H$ . However, previous numerical work mainly focused on the beam and ES waves [6], and very recently on emission in a homogeneous plasma [7], quantitative studies of emission in inhomogeneous plasma are lacking. The second aim of the Letter is to numerically study type-III bursts more realistically, incorporating density fluctuations, which are key to lead to a SGT state.

In this Letter, we report the first simulations of type-III bursts that account for beam propagation, and ES and EM wave generation. We include microscale quasilinear and nonlinear interactions, incorporate intermediate-scale ambient density inhomogeneities, and consider large scale evolution of beams, and ES and EM waves. Moreover, we compare Langmuir field statistics with SGT predictions. This represents a significant advance in modeling type-III phenomena in realistic nonuniform plasmas.

The electron distribution function  $f(t, x, v)$  and Langmuir wave occupation number  $N_L(t, x, k)$  obey

$$\frac{\partial f(t, x, v)}{\partial t} + v \frac{\partial f(t, x, v)}{\partial x} = \frac{\partial}{\partial v} [A_L f(t, x, v)] + \frac{\partial}{\partial v} \left[ D_L \frac{\partial f(t, x, v)}{\partial v} \right] + S_b, \quad (1)$$

$$\frac{\partial N_L(t, x, k)}{\partial t} + v_g \frac{\partial N_L(t, x, k)}{\partial x} - \frac{\partial \omega_L}{\partial x} \frac{\partial N_L(t, x, k)}{\partial k} = \alpha_L + \gamma_L N_L(t, x, k) - \gamma_L^d N_L(t, x, k) + R_L, \quad (2)$$

respectively. Here 1D quasilinear equations are used, due to computational limitations. However, the spectra of 3D  $L$  waves (and  $S$  waves, discussed below) which are involved in ES and EM processes (ii)–(iv) are approximated by parametrizing the angular distribution using 1D spectra from (2) and assuming conservation of occupation numbers in 3D and 1D, for axially symmetric (in the beam or the  $x$  direction) ES decay process [7]. The variables  $x$  and  $v$  denote position and speed at time  $t$ ,  $k$  is  $L$  wave number parallel to the beam velocity, and is related to  $v$  via the Cerenkov resonance condition  $\omega_L = kv$ . The Langmuir dispersion relation is  $\omega_L^2 = \omega_p^2 + 3k^2v_e^2$ ,  $v_g = \partial\omega_L/\partial k$  is the group speed,  $\omega_p = (ne^2/m\epsilon_0)^{1/2}$ ,  $v_e = (k_B T_e/m)^{1/2}$ , and  $m$ ,  $e$ ,  $T_e$ , and  $n$  are electron mass, charge, temperature, and number density, respectively. Equation (2) assumes the geometrical optics approximation and negligible density fluctuation effects on the Langmuir dispersion relation; both assumptions are valid for the weak, relatively large spatial scale, density fluctuations relevant here. The coefficients  $A_L$ ,  $D_L$ ,  $\alpha_L$ , and  $\gamma_L$ , describing spontaneous emission and quasilinear interactions, are given in [7]. The source term  $S_b$  in (1) represents local heating of a fraction  $F_{acc}$  of particles from  $T_e$  to  $T_h$  ( $> T_e$ ) over a characteristic region of width  $(\delta t, \delta x)$  centered at  $(t_0, x_0)$ , which leads to formation of a beam due to time-of-flight effects [7]:

$$S_b = F_{acc}(\sqrt{\pi}\delta t)^{-1}[f_h(v, T_h) - f_c(v, T_e)] \times \exp[-(t - t_0)^2(\delta t)^{-2} - (x - x_0)^2(\delta x)^{-2}]. \quad (3)$$

The speed dependence of  $f_h$  and  $f_c$  is assumed to be Maxwellian. The effective 3D ES decay rate  $R_L$  in (2) was discussed in [7]. The last term on the left side of (2) describes refraction of  $L$  waves due to density gradients. The term  $\gamma_L^d N_L$  in (2) represents effective 3D damping due to Langmuir scattering off density fluctuations.

$$\partial N_T(t, x, k_T)/\partial t + v_T \partial N_T(t, x, k_T)/\partial x - [\partial\omega_T/\partial x] \partial N_T(t, x, k_T)/\partial k_T = R_T. \quad (6)$$

Here  $\omega_T^2 = \omega_p^2 + (k_T^2 + k_\rho^2)c^2$ ,  $v_T = \partial\omega_T/\partial k_T$ , and  $R_T$  are the  $T$  wave group speed and emission rate, respectively. The effective 3D source term  $R_T$  is obtained by integrating 3D EM emission rates in [7] over  $k_\rho$ . Remotely generated radiation due to propagation of source emissions from elsewhere are represented via terms related to  $v_T$  and  $\partial\omega_T/\partial x$ , which are approximated by averaging over the 3D source emission region and emission angle.

For remotely generated radiation, it is convenient to consider ingoing ( $k_T < 0$ ) and outgoing ( $k_T > 0$ ) emissions separately, based on insights obtained by tracing representative rays in 3D for  $n_0(x) \sim x^{-2}$ . First, at a given  $x$ , the characteristics of remotely generated ingoing radiation are different for  $F$  and  $H$  waves. This harmonic ( $H$ ) emission is due to radiation propagating with  $k_H < 0$  from locations with larger  $x$ . However, remotely generated ingoing fundamental ( $F$ ) emission is negligible due to almost imme-

diately reflection by the density gradient after rays with  $k_F < 0$  are emitted. Second, remotely generated outgoing radiation are attributed to the propagation of two types of rays: those with initial  $k_T > 0$  from smaller  $x$ , and others with initial  $k_T < 0$  that have been reflected. We approximate the angular patterns of the source emissions to be dipolar and quadrupolar for  $F$  and  $H$  waves, respectively, consistent with previous analytic work and our results for a homogeneous plasma [7].

$$\gamma_L^d(k) = \frac{\pi}{12} \frac{g}{\Theta^2} \frac{\omega_p}{k_D k_f} \left(\frac{k_D}{k}\right)^3 \frac{1}{n_0^2} \left(\frac{\partial n_1}{\partial x}\right)^2, \quad (4)$$

with  $n_0(x)$  the time-averaged density and  $n_1(t, x)$  the fluctuating part. Here  $n_1(t, x)$  constitutes  $S$  wave turbulence, with rms level  $n_{1\text{rms}}$ , characteristic spatial scale  $l$  or wave number  $k_f = 2\pi/l \ll k < k_D$  (the Debye wave number), and temporal scale  $\tau$ , which are independent of beam and  $L$  waves. Our calculations show  $g \approx 5.8$  instead of  $g = 1$ , as given in [9]. The polar angular range occupied by the  $L$  wave vectors is  $\Theta \approx 0.5$  [10].

The ion sound wave evolution is described by

$$\frac{\partial N_S(t, x, k)}{\partial t} + v_S \frac{\partial N_S(t, x, k)}{\partial x} = \alpha_S - \gamma_S N_S(t, x, k) + R_S. \quad (5)$$

Here  $N_S$  is the occupation number, and  $v_S$ ,  $\alpha_S$ ,  $\gamma_S$ , and the effective 3D  $S$  wave emission rate  $R_S$  depend on ion temperature  $T_i$  and other quantities [7].

To study EM emission in an inhomogeneous plasma, we need to consider propagation effects such as refraction and reflection (scattering is neglected here). Assuming stratification in the  $x$  direction, EM waves  $T$  ( $= F$  or  $H$ ) depend on  $x$  and wave numbers  $k_T$  and  $k_\rho$  which are in the  $x$  and perpendicular directions, respectively. We examine the  $T$  wave dynamics as a function of  $t$ ,  $x$ , and  $k_T$  by integrating over the dependence on  $k_\rho$ . In the geometric optics approximation, the evolution of the  $T$  wave occupation number  $N_T(t, x, k_T)$  obeys

diately reflection by the density gradient after rays with  $k_F < 0$  are emitted. Second, remotely generated outgoing radiation are attributed to the propagation of two types of rays: those with initial  $k_T > 0$  from smaller  $x$ , and others with initial  $k_T < 0$  that have been reflected. We approximate the angular patterns of the source emissions to be dipolar and quadrupolar for  $F$  and  $H$  waves, respectively, consistent with previous analytic work and our results for a homogeneous plasma [7].

We employ similar techniques to [7] for solving (1), (2), (5), and (6). Because of the need to resolve density fluctuations and have systems large enough to allow development of interesting physics, the simulation domains are made about 100 times larger than the typical spatial scale  $l$  of  $n_1$ . Then  $l$  is much larger than actually observed in the solar wind [e.g., at 1 a.u.,  $l$  is  $\sim 10^3$  times the mean length scale  $\sim 10^6$  m observed [5]], but still much smaller than the scale of solar wind expansion.

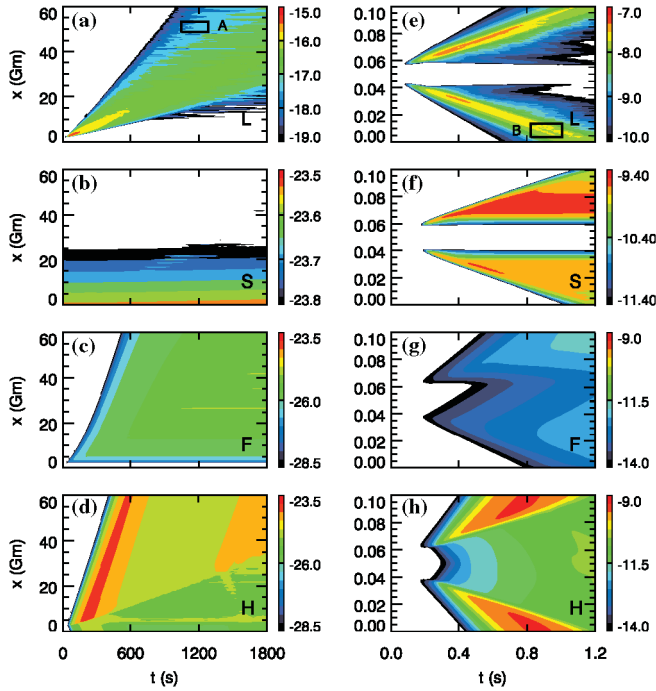


FIG. 1 (color). Energy density  $\log_{10}[W/(1 \text{ Jm}^{-3})]$  for (a) and (e)  $L$ , (b) and (f)  $S$ , (c) and (g)  $F$ , and (d) and (h)  $H$  waves at 1 a.u. (left column) and the corona (right column) for the parameters in Table I. A and B label rectangles discussed in text relevant to Fig. 3.

Figure 1 shows the evolution of the energy density of the four wave modes, by integrating  $N_M(t, x, k_M)\hbar\omega_M$  over  $k_M$  ( $M = L, S, F$  or  $H$ ), for IP conditions shown in Table I at 1 a.u. and in the corona. For the coronal event, heating occurs for both  $v > 0$  and  $v < 0$ , while for the 1 a.u. event, heating is only for  $v > 0$ .

At 1 a.u., Langmuir waves in Fig. 1(a) fill a “fan” in coordinate space after the source injection. This occurs due to time-of-flight beam formation, quasilinear interactions between beam and  $L$  waves, and ES decay of the  $L$  waves. Figure 1(a) shows that the  $L$  waves vary irregularly with  $t$  and  $x$ . This sporadic behavior is produced predominantly by random damping associated with density fluctuations, as discussed below. Figure 1(a) also shows that irregularities in the  $L$  wave levels are larger at larger  $x$ . The  $S$  waves in Fig. 1(b) also show some degree of irregularity, consistent with observations [11]. This clumpiness occurs because, first,  $S$  waves are generated via successive ES decays  $L_i \rightarrow L_{i+1} + S_{i+1}$  ( $i = 0, 1$ ) of the most intense  $L$  waves which are bursty; second, the speed of the  $S$  waves is small, so they stay in clumps.

The  $F$  and  $H$  waves in Figs. 1(c) and 1(d) are generated via EM decays  $L_i \rightarrow F_{i+1} + S_{i+1}$  of, and coalescences  $L_i + L_{i+1} \rightarrow H_{i+1}$  between, beam-driven waves  $L_0$  and product waves  $L_1$  and  $L_2$  from the ES decays, respectively, where  $i = 0, 1$ . Figure 1(c) shows that the  $F$  emission has one peak, while  $H$  emission in Fig. 1(d) has two peaks: one starts at  $t \approx 200$  s (red level) and the other at  $t \approx 1400$  s (orange level). The first peak is generated by  $L_0 + L_1 \rightarrow H_1$ . The other peak is due to two coalescence processes occurring at  $x = (27\text{--}30)$  Gm:  $L_0 + L_1 \rightarrow H_1$  between  $L_0$  and  $L_1$  waves which are strongly spatially localized due to density fluctuations, and  $L_1 + L_2 \rightarrow H_2$ , with the former being dominant. In contrast to the clumpy ES waves, the EM emissions vary smoothly. This occurs because the EM waves have much larger group speeds than the ES waves.

The  $T$  waves propagate both forward and backward. Forward propagation is evident in regions ( $x \geq x_0$ ) downstream of the injection site (e.g., where  $L$  waves are thermal before the beam arrives). For  $H$  waves, backward propagation is illustrated by the presence of  $H$  waves at upstream locations ( $x \leq x_0$ ). Because of immediate reflection of the backward propagating  $F$  waves, upstream  $F$  emission is negligible. In addition, due to the different angular emission patterns and propagation speeds of the  $F$  and  $H$  waves [e.g.,  $v_F(x) \approx (6\text{--}99)v_e$ , while  $v_H(x) \approx (88\text{--}95)v_e$ ], detailed variations of the  $F$  waves in  $tx$  space are smeared out and we see only one peak. Moreover, at 1 a.u. both  $F$  and  $H$  emissions are important:  $H$  emission dominates at early times, and both  $F$  and  $H$  radiation occur later.

Figures 1(e) and 1(f) for the corona show the  $L$  and  $S$  wave levels are much higher than at 1 a.u. The level of the  $S$  waves relative to  $L$  waves is larger in the corona than at 1 a.u. This is due to the larger ratio  $T_i/T_e$  in the corona and the sensitivity of ES decay to this ratio [7]. Figures 1(g) and 1(h) show that  $H$  emission dominates  $F$  emission (with the maximum 120 times higher), and both  $F$  and  $H$  emissions in the upward direction are stronger than downward, all consistent with observations and theory [2,5]. This asymmetry is due to downward beam narrowing in velocity space, as discussed below.

Figure 2 shows the electron distribution function for the coronal case at  $x_a$  and  $x_b$ , symmetric about  $x_0$ . The beams evolve toward smaller speeds with time. Meanwhile, detailed examination shows that the beam is wider at the upward location  $x_b$  than the downward position  $x_a$ , consistent with theory [5]. At  $t = 0.80$  s, Fig. 2 also shows the development of mini-plateaus at large speeds in both directions. This is due to thermal particles absorbing energy

TABLE I. Assumed source and plasma parameters at the corona and 1 a.u.

Quantity	$T_e$	$T_i/T_e$	$n_0(x=0)$	$n_{1 \text{ rms}}/n_0$	$l$	$\tau$	$T_h$	$F_{acc}$	$t_0$	$\delta_i/t_0$	$x_0$	$\delta_x/x_0$
Corona	2.0	0.5	$9.0 \times 10^{14}$	0.5	0.0021	$7.3 \times 10^{-3}$	25	$5.0 \times 10^{-5}$	$2.0 \times 10^{-2}$	0.25	0.05	0.04
1 a.u.	0.17	0.2	$7.0 \times 10^6$	0.2	0.84	$3.5 \times 10^1$	25	$5.0 \times 10^{-5}$	$1.8 \times 10^1$	0.01	2.0	0.08
Unit	MK	...	$\text{m}^{-3}$	%	Gm	s	MK	...	s	...	Gm	...

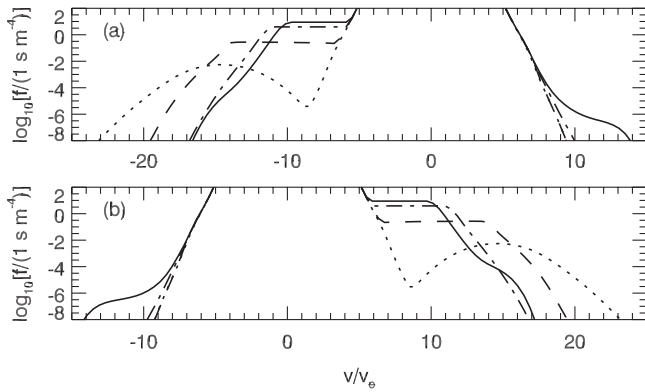


FIG. 2. Particle distribution function  $f(v)$  at (a)  $x_a = 0.015$  Gm and (b)  $x_b = 0.085$  Gm at various times for the coronal conditions. Dotted line:  $t = 0.40$  s, dashed line:  $t = 0.56$  s, dot-dashed line:  $t = 0.72$  s, and solid line:  $t = 0.80$  s.

from product  $L$  waves generated by multiple (three here) ES decays. Also, in contrast to large variations in  $L$  wave levels, the beam distribution function only varies gradually with  $v$  and  $t$  because  $L$  levels are directly modulated by density fluctuations, whereas the beam is only affected indirectly via beam- $L$  wave resonant interactions. The smooth variation in the beam distribution is consistent with observations [11], and implies weak irregularity in the beam slope. Consequently, clumpiness in the  $L$  waves is due mainly to randomness in  $\gamma_L^d$ , rather than stochasticity in the beam slope, at least for the present parameters. We also find (not shown) that density fluctuations cause slower quasilinear relaxation of the beam, in qualitative agreement with theory [4,8]: when density fluctuations are present, beam energy cannot be effectively absorbed by  $L$  waves, which are shifted to regions out of resonance with the beam, so the beam lasts longer. On average, the beam speed is almost the same as for the uniform case, which verifies an analytic prediction for the validity of the quasilinear description for clumpy  $L$  waves [12].

Statistical analysis of  $L$  wave fields probes the mechanisms underlying burstiness. In our simulations, beam speed varies with  $x$  and  $t$ , so the quantity directly comparable with SGT is not the gain  $G$  of  $L$  waves but a reduced gain  $X = (G - \langle G \rangle) / \sigma_G$ , where  $G = \ln(W_L / W_{L\theta})$ ,  $\langle G \rangle$  and  $\sigma_G$  are the average and standard deviation of  $G$ , respectively, and  $W_{L\theta}$  is thermal  $L$  energy density [4]. SGT predicts a distribution  $P(X) = (2\pi)^{-1/2} \exp(-X^2/2)$ . Figures 3(a) and 3(b) show  $P(X)$  for the  $L$  energy at 1 a.u. and in the corona, respectively. Good agreement between data and the predicted  $P(X)$  is evident at intermediate  $X$ . A lower bound is imposed by the thermal level. A cutoff at high  $X$  is found to be due to a saturation level set by the beam free energy.

We find that varying the level and spatial scale of density fluctuations modifies the results appreciably. Larger  $n_{1\text{rms}}$  and/or smaller  $l$  enhances effective damping of  $L$  waves and thus all wave levels are lower and  $L$  waves are burstier. Source parameters also affect the results; e.g., larger  $T_h$

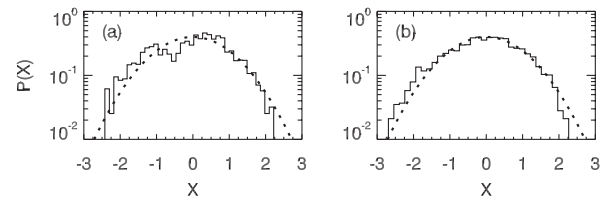


FIG. 3. Probability distribution  $P(X)$  of the  $L$  waves at (a) 1 a.u. and (b) corona in Regions A and B in Figs. 1(a) and 1(e), respectively. Dotted curve shows the SGT prediction.

and/or  $F_{acc}$  increase the wave levels. In addition, our studies suggest that  $H$  emission generally dominates at small heliocentric distances ( $\lesssim 3R_\odot$ ); at large distances, both  $F$  and  $H$  emissions can be important or one may dominate, depending on the source parameters, consistent with observations and theory [1,5,11].

We have presented the first numerical simulations of type-III bursts in the inhomogeneous solar and IP plasma, including beam and wave dynamics, density fluctuations, and large scale propagation. Simulations confirm SGT predictions, and agree qualitatively with observations and theory. This work has significant implications for the space and astrophysical phenomena discussed at the start of this Letter. Future work will assess EM wave scattering off density fluctuation effects and consider even more realistic 3D conditions.

- 
- [1] A. O. Benz, *Plasma Astrophysics* (Kluwer, Dordrecht, 2002), 2nd ed.; V. L. Ginzburg and V. V. Zheleznyakov, *Soviet Astron.* **2**, 653 (1958); I. H. Cairns and M. L. Kaiser, in *The Review of Radio Science 1999–2002*, edited by W. R. Stone (Wiley-IEEE Press, New York, 2002), p. 749.
  - [2] M. J. Aschwanden, A. O. Benz, and R. A. Schwartz, *Astrophys. J.* **417**, 790 (1993).
  - [3] I. H. Cairns, *Planet. Space Sci.* **52**, 1423 (2004).
  - [4] P. A. Robinson, *Sol. Phys.* **139**, 147 (1992); P. A. Robinson, I. H. Cairns, and D. A. Gurnett, *Astrophys. J.* **407**, 790 (1993); P. A. Robinson, B. Li, and I. H. Cairns, *Phys. Rev. Lett.* **93**, 235003 (2004).
  - [5] P. A. Robinson and I. H. Cairns, *Sol. Phys.* **181**, 363 (1998); P. A. Robinson and A. O. Benz, *ibid.* **194**, 345 (2000).
  - [6] R. J. M. Grogard, in *Solar Radiophysics*, edited by D. J. McLean and N. R. Labrum (Cambridge University Press, Cambridge, England, 1985), p. 253; E. P. Kontar and H. L. Pecseli, *Phys. Rev. E* **65**, 066408 (2002).
  - [7] B. Li, A. J. Willes, P. A. Robinson, and I. H. Cairns, *Phys. Plasmas* **12**, 012103 (2005); **12**, 052324 (2005).
  - [8] K. Nishikawa and D. D. Ryutov, *J. Phys. Soc. Jpn.* **41**, 1757 (1976).
  - [9] D. B. Melrose, *Sol. Phys.* **111**, 89 (1987).
  - [10] P. A. Robinson, A. J. Willes, and I. H. Cairns, *Astrophys. J.* **408**, 720 (1993).
  - [11] R. P. Lin, W. K. Levedahl, W. Lotko, D. A. Gurnett, and F. L. Scarf, *Astrophys. J.* **308**, 954 (1986).
  - [12] D. B. Melrose and N. F. Cramer, *Sol. Phys.* **123**, 343 (1989).